

On the benefit of aberration-corrected HAADF-STEM for strain determination and its application to tailoring ferroelectric domain patterns

Y.L. Tang¹, Y.L. Zhu¹, X.L. Ma^{*}

Shenyang National Laboratory for Materials Science, Institute of Metal Research, Chinese Academy of Sciences, Wenhua Road 72, 110016 Shenyang, China

ARTICLE INFO

Article history:

Received 16 September 2014
 Received in revised form
 21 September 2015
 Accepted 26 September 2015
 Available online 30 September 2015

Keywords:

Aberration-corrected scanning transmission electron microscopy
 High angle annular dark field (HAADF)
 Strain determination
 Geometrical phase analysis (GPA)
 Ferroelectric domain structure
 PbTiO₃ films

ABSTRACT

Revealing strains on the unit-cell level is essential for understanding the particular performance of materials. Large-scale strain variations with a unit-cell resolution are important for studying ferroelectric materials since the spontaneous polarizations of such materials are strongly coupled with strains. Aberration-corrected high-angle-annular-dark-field scanning transmission electron microscopy (AC-HAADF-STEM) is not so sensitive to the sample thickness and therefore thickness gradients. Consequently it is extremely useful for large-scale strain determination, which can be readily extracted by geometrical phase analysis (GPA). Such a combination has various advantages: it is straightforward, accurate on the unit-cell scale, relatively insensitive to crystal orientation and therefore helpful for large-scale. We take a tetragonal ferroelectric PbTiO₃ film as an example in which large-scale strains are determined. Furthermore, based on the specific relationship between lattice rotation and spontaneous polarization (P_s) at 180° domain-walls, the P_s directions are identified, which makes the investigation of ferroelectric domain structures accurate and straightforward. This method is proposed to be suitable for investigating strain-related phenomena in other ferroelectric materials.

© 2015 Elsevier B.V. All rights reserved.

1. Introduction

Strain determination on the unit-cell scale is essential for understanding many physical behaviors of materials, and such strains can be readily extracted by conventional high resolution transmission electron microscopy (HRTEM). For instance, HRTEM imaging was successfully employed to measure unusual surface lattice expansion of nanoporous gold, which is essential for its high catalytic activity [1]; HRTEM was also used for mapping strain interactions between Si channel and Si₈₀Ge₂₀ source in strained silicon transistors, which is important for clarifying the strain modulated carrier behaviors [2]. In addition, there were abundant applications of HRTEM for analyzing strain behaviors at interfaces, grain boundaries and defects, helping to improve the understanding of relevant mechanical or functional properties [3–9]. Indeed, HRTEM has been proved to be an accurate method in a TEM for local strain measurements [10]. Nevertheless, for large area strain analysis, HRTEM imaging is sensitive to the local specimen thickness and frequently meets with the contrast-reversal

problem, rendering the image interpretation complicated [11]. Moreover, the contrast-reversal problem could be aggravated for samples containing heavy elements [10,11]. Such problems could embarrass the *large area* strain analysis of many technologically important materials on the unit-cell scale, e.g. perovskite ferroelectric/multiferroic oxides in which strain is essential for understanding the ferroelectric/piezoelectric behavior [12,13].

Imaging with an aberration-corrected high angle annular dark field scanning transmission electron microscope (AC-HAADF-STEM) has become a powerful technique to study crystal structures at sub-angstrom resolution [14–28]. Although the HAADF-STEM imaging mechanism is complicated, a generally Z^n depended atomic contrast could be observed, which makes the interpretation of the images straightforward (where Z is the atomic number, and $n \approx 1.7$, close to the asymptotic Rutherford scattering limit of $Z=2$) [24–28]. Moreover, due to its incoherent essence, there is no contrast reversal in the HAADF-STEM images, regardless of the sample thickness and some small variety of defocus value [14,15,24,28]. In addition, the aberration-corrected convergent electron probe current is strong enough to penetrate thick samples containing elements with medium mass (SrTiO₃), even when the thickness exceeds 100 nm [29], where a HAADF-STEM image with little resolution compromise and no contrast reversal effect can still be obtained [24,29,30].

^{*} Corresponding author. Fax: 86 24 23891320.

E-mail address: xlma@imr.ac.cn (X.L. Ma).

¹ Authors contributed equally in this work.

The advantages of AC-HAADF-STEM make it very useful for large-area strain analysis. Moreover, improving spatial resolution of a TEM instrument could further enlarge the fields of view in a high resolution HAADF-STEM image. This is important for strain-related physical property analysis because large areas always contain more useful information, such as the strain of domain-walls in ferroelectrics. The strains in these large area images can be easily extracted by geometrical phase analysis (GPA) [2,7–9,23,31–36]. Thanks to the low sensitivity of HAADF-STEM images to thickness/defocus values [14,15,24,28], no superfluous ‘geometrical phase variations’ can be introduced by defocus and/or thickness gradient, which is a precondition to perform GPA and other strain analysis [31,33,34].

In this paper, large-scale strains in $\text{PbTiO}_3/\text{SrTiO}_3$ multi-layers and at 180° domain-walls therein are analyzed based on AC-HAADF-STEM images. We show the great advantage of a combination of AC-HAADF-STEM and GPA, as exemplified by extracting domain patterns in ferroelectric PbTiO_3 films.

2. Material and methods

The $\text{PbTiO}_3/\text{SrTiO}_3$ multilayers were deposited on SrTiO_3 substrates by pulsed laser deposition (PLD), using a Lambda Physik LPX 305i KrF ($\lambda=248$ nm) excimer laser. The background pressure was 10^{-5} Pa and the substrate temperature was kept at 650°C . During the growth of the PbTiO_3 layers, an oxygen pressure of 20 Pa, a laser repetition rate of 5 Hz and a laser energy density of 2 J cm^{-2} were used [37]. Cross-sectional samples for the STEM experiments were prepared by slicing, gluing, grinding, dimpling, and finally ion milling. A Gatan PIPS was used for the final ion milling. AC-HAADF-STEM images were recorded using an aberration-corrected scanning transmission electron microscope (Titan Cubed 60–300 kV microscope (FEI) fitted with a high-brightness field-emission gun (X-FEG) and double Cs corrector from CEOS) operating at 300 kV. The diffraction contrast image was recorded using a conventional TEM (Tecnai G2 F30 (FEI) working at 300 kV). The acquisition durations of all HAADF-STEM images used here were 40 s. The dwell time and sampling rate are about $40\ \mu\text{s}$ and $2.5 \times 10^4/\text{s}$, respectively. The beam convergence angle is 25 mrad, and the collection angle ranges from 50 mrad to 250 mrad. Strain fields were deduced by using custom plugins of GPA for Gatan DigitalMicrograph [31]. The visualization of the strains and lattice rotations was carried out using Gatan DigitalMicrograph software.

3. Results

3.1. General information

At room temperature, PbTiO_3 crystal has a tetragonal structure with lattice parameters $a=b=3.900\ \text{\AA}$ and $c=4.148\ \text{\AA}$ [38]. The SrTiO_3 substrate has a cubic structure with lattice parameter $a=3.905\ \text{\AA}$ [39]. The c -oriented $\text{PbTiO}_3/\text{SrTiO}_3$ heterointerface has very little strain due to the small lattice mismatch ($<0.13\%$). Such a heteroepitaxial system also minimizes the strain effects of the substrates on studying the strains of 180° domain-walls in PbTiO_3 .

To produce 180° domain-walls in the PbTiO_3 layers and thus show the usefulness of the combination of AC-HAADF-STEM and GPA, a two-layer PbTiO_3 structure sandwiched by insulating SrTiO_3 layers was fabricated. The insulating SrTiO_3 layers isolate the PbTiO_3 layers from possible external charges, thus promote the formation of 180° domain-walls [40].

Generally, 180° domain-walls in tetragonal PbTiO_3 crystal have dipoles across the domain-walls arranged as 180° configurations [3,12,41,42]. The 180° domain-wall extends along $\{100\}$ plane [42],

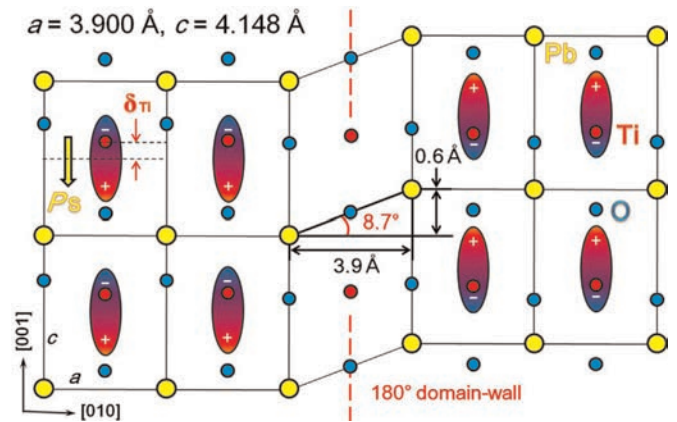


Fig. 1. Illustration of 180° domain-wall in ferroelectric PbTiO_3 lattice. The spontaneous polarization (P_s , marked by yellow arrow) of the PbTiO_3 unit-cells is caused by relative displacements of the O^{2-} and Ti^{4+} , Pb^{2+} ions exhibiting as off-center shifts of Ti^{4+} anions, as marked by δ_{Ti} . The tetragonality (c/a) of the PbTiO_3 unit-cell is magnified here for visualization. Oppositely arranged P_s and δ_{Ti} beside a 180° domain-wall would induce a $0.6\ \text{\AA}$ relative shift of the Pb^{2+} lattice accompanied by an 8.7° lattice rotation, as indicated at the domain-wall.

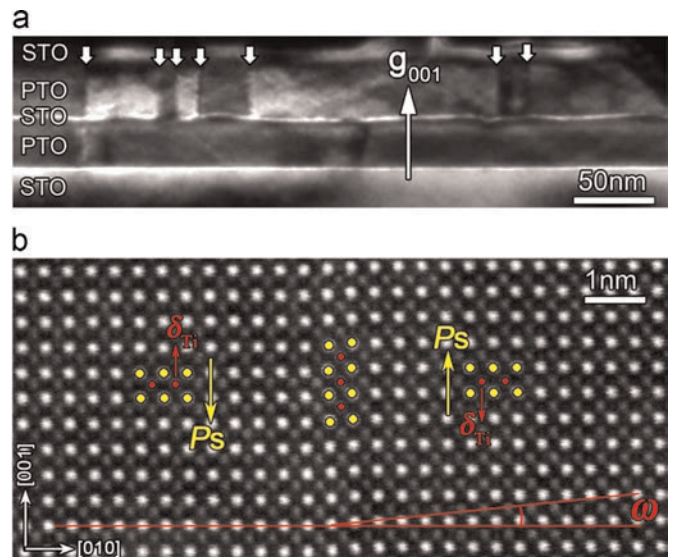


Fig. 2. Experimental images of 180° domain-walls in PbTiO_3 . (a) Dark field TEM image of the $\text{PbTiO}_3/\text{SrTiO}_3$ multilayer showing the 180° domains. (b) AC-HAADF-STEM images of a 180° domain-wall in PbTiO_3 . The insets show the shifts of Ti^{4+} column (red) relative to the Pb^{2+} columns (yellow), which are opposite to the P_s directions of respective domains, as marked by yellow arrows. Note the lattice rotation across the 180° domain-wall, indicated by ω , which is consistent with the lattice rotation model shown in Fig. 1.

as shown in Figs. 1 and 2. Theoretical simulation predicted that the relative displacement along $[001]$ of the Pb^{2+} lattice on both side of the 180° domain-walls is about $0.6\ \text{\AA}$ [43], and this was further confirmed by aberration corrected HRTEM observations under negative spherical aberration condition [41]. If the width of the 180° domain-walls is one unit-cell, then this displacement will cause a lattice rotation of about 8.7° across the domain-wall (Fig. 1), which should be detectable by using GPA. However, in real PbTiO_3 crystals, the magnitude of this rotation might be decreased because the width of a 180° domain-wall sometimes exceeds one unit-cell [43]. In addition, the dipoles formed by the relative shifts of anions (O^{2-}) and cations (Pb^{2+} and Ti^{4+}) are also schematically illustrated in Fig. 1, which is typically accompanied by Ti^{4+} off-

center displacements from the Pb^{2+} lattice, as marked by δ_{Ti} . The dipole direction (P_s) is opposite to the δ_{Ti} , as the yellow arrow indicates [3,41,42].

3.2. Strain analysis based on AC-HAADF-STEM and GPA

Fig. 2(a) is a representative dark field TEM image of 180° domains in PbTiO_3 (PTO). Vertical boundaries between the white and dark contrast in the first PTO layer indicate the 180° domain-walls, as marked with downward arrows. One of the 180° domain-walls is further magnified in AC-HAADF-STEM mode, as shown in Fig. 2(b). The dipoles formed by the Ti^{4+} off-center displacements beside the 180° domain-wall can be identified. This 180° configuration of P_s directions must indicate a 180° domain-wall between them. As above mentioned, there are several degrees of lattice rotation across the 180° domain-wall, and this is indeed visible in the HAADF-STEM image. The relative shifts of Pb^{2+} lattice beside the 180° domain-wall were indicated by three relatively sheared unit-cells at the domain-wall, and the resultant lattice rotation can be identified, as marked by the red lines (ω in Fig. 2(b)).

As is seen in Fig. 2(b), atomic-scale information is displayed in the aberration corrected STEM images with very high magnification—not only the strains (lattice rotation), but also the ferroelectric ion shifts (δ_{Ti}). However, there is an intrinsic drawback of highly magnified TEM images—the areas of these images are

extremely limited, for instance, ranging within $20 \text{ nm} \times 20 \text{ nm}$; and the area may become even smaller if the magnification is further enhanced to obtain extremely subtle atomic details (for instance, the size of the raw image corresponding to Fig. 2(b) is $12.9 \text{ nm} \times 12.9 \text{ nm}$). Thus the information contained in highly magnified images is also restricted. An understanding of ferroelectric performance is gained not only from atomic-scale details but also other physical properties such as their ferroelectric domain patterns [12,13,40]. Fortunately, GPA has shown great potential to extract strain information in high resolution AC-HAADF-STEM images with large field of view [23,31–34]. The accuracy of GPA for determining displacement fields can reach 0.03 \AA , even without the aid of aberration corrected TEM [32]. Its efficiency was corroborated in 2011 by Catalan et al. to quantitatively determine the gradual and continuous variety of strains in PTO lattice obtained by high resolution AC-HAADF-STEM with large field of view [23]. For extracting strain information in these images, AC-HAADF-STEM based GPA analysis exhibits advantages over direct methods which are based on ‘peak finding’ in the real space images [4,6,31,34], because the pixel size in these images (with large field of view) is too large to be accurately located (will be further elaborated in Fig. 5(f)).

It should be emphasized that the lattice rotation across the 180° domain-wall in PTO can be treated as a fingerprint for determining the P_s directions beside the domain-wall. We define a

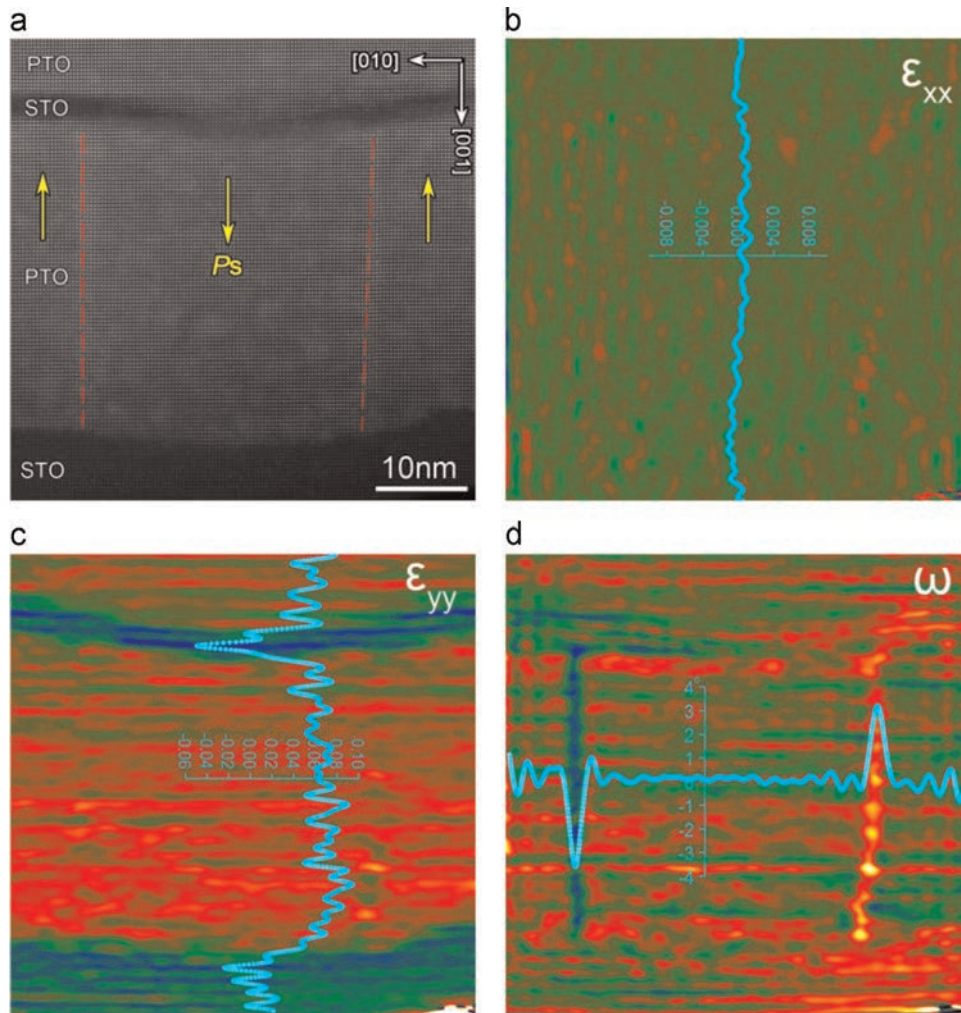


Fig. 3. AC-HAADF-STEM based 2D strain mappings of the $\text{PbTiO}_3/\text{SrTiO}_3$ multilayer in low magnified image. (a) An AC-HAADF-STEM image containing 180° domain-walls. (b) In-plane strain ϵ_{xx} . (c) Out-of-plane strain ϵ_{yy} . (d) Lattice rotation mapping ω . The insets in (b), (c) and (d) are corresponding line-profiles. The scanning direction is up to bottom. The radius of mask size used here is 0.8 1/nm .

counterclockwise lattice rotation as a positive rotation. Fig. 2 (b) shows the positive rotation example for the 180° domain-wall. The left domain exhibits downward P_s while the right domain exhibits upward P_s . So the strain information across the 180° domain-walls in PTO is enough to determine P_s directions in each ferroelectric domain and thus the domain patterns. In other words, the atomic scale information, such as ferroelectric ion displacements (δ_{Ti}) is not necessary for the determination of P_s directions. We will use two examples to clarify the determination process of domain patterns in PTO.

Fig. 3(a) shows an AC-HAADF-STEM image of the $\text{PbTiO}_3/\text{SrTiO}_3$ multilayer. The size of this image is about $50 \text{ nm} \times 50 \text{ nm}$. For this magnification, it becomes difficult to inspect the P_s configurations by identifying δ_{Ti} in the PTO layer because it was somewhat concealed by the corresponding bigger pixel size (will be further elaborated in Fig. 5(e)). Instead, attempts through the fingerprint of 180° domain-wall were performed by GPA. The orientation of the PTO layer was first checked by lattice parameter changes. The horizontal strain (ϵ_{xx}) is shown in Fig. 3(b). The basically uniform distribution of ϵ_{xx} indicates all the PTO unit-cells were a -oriented along the horizontal direction (the a lattice of PTO is almost equal to lattice parameter of SrTiO_3). Thus all the PTO layers were c -oriented along vertical direction. This inference can be further approved by checking the vertical strain (ϵ_{yy}) shown in Fig. 3(c). Sharp fluctuation of ϵ_{yy} across the $\text{PbTiO}_3/\text{SrTiO}_3$ interfaces can be clearly seen, since the c lattice parameter of PTO is much bigger than that of SrTiO_3 . The efficiency of GPA performed on this HAADF-STEM image can be assessed by comparison of the image contrast and ϵ_{yy} : the bending of the $\text{PbTiO}_3/\text{SrTiO}_3$ interfaces is

consistent with each other in both Fig. 3(a) and (c). Finally, Fig. 3 (d) shows the lattice rotation map of Fig. 3(a). Two vertical bands can be observed, which indicate some unusual lattice rotation along the vertical direction. These two distinct bands exhibit obvious opposite contrast. Since the other uniform area (PTO unit cells between the two vertical bands) was selected as reference lattice with 0 rotation, the opposite contrast of the two vertical bands must indicate a negatively and a positively rotated lattice band, respectively. Moreover, these lines were traced along c direction of the PTO lattice. So it is reasonable to infer that they are 180° domain-walls, and this inference was indeed confirmed by high-magnification AC-HAADF-STEM images as Fig. 2(b). Although some scanning noise is distinguishable in the ϵ_{yy} and ω maps (horizontal fluctuations in Fig. 3(c) and (d)) due to the inevitable scanning error of the STEM imaging mode, the vertical strain of the multilayer and the lattice rotation across the 180° domain are less affected and well detectable.

Since the signs (positive or negative) of the lattice rotation across the 180° domain-wall in PTO can serve as a fingerprint for the nearby P_s directions, it is now feasible to determine domain patterns contained in the PTO layer, *without* the aid of ionic position information. As above mentioned in Fig. 2(b), positive rotation indicates downward and upward P_s in the left and right domain, respectively, and vice versa. Thus the domain configuration of the sandwiched PTO layer can be uniquely determined, as the yellow arrows in Fig. 3(a) indicate.

The efficiency of this method can be further confirmed by an image with extremely low magnification. Fig. 4(a) shows an AC-HAADF-STEM image of the $\text{PbTiO}_3/\text{SrTiO}_3$ multilayer. One can see

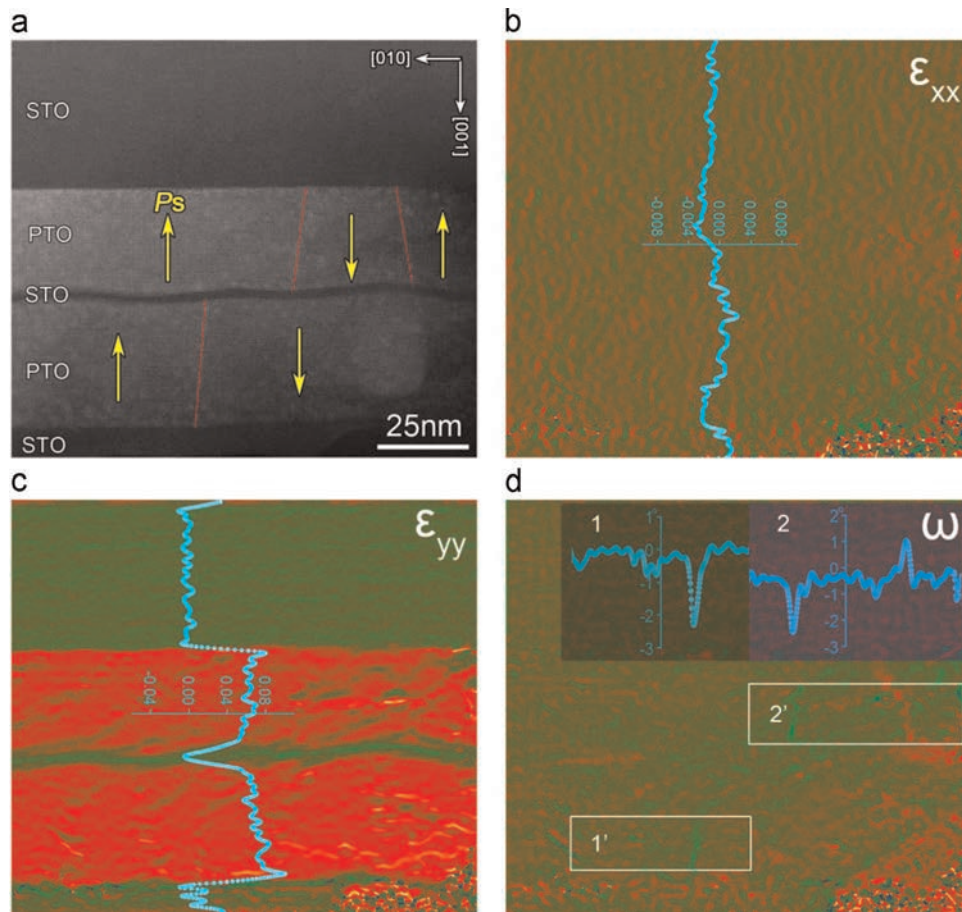


Fig. 4. AC-HAADF-STEM based 2D strain mappings of the $\text{PbTiO}_3/\text{SrTiO}_3$ multilayer at extremely low magnified image. (a) HAADF-STEM images of the whole $\text{PbTiO}_3/\text{SrTiO}_3$ containing 180° domain-walls. (b) In-plane strain ϵ_{xx} . (c) Out-of-plane strain ϵ_{yy} . (d) Lattice rotation mapping ω . The insets in (b)–(d) are corresponding line-profiles. The scanning direction is up to bottom. The radius of mask size used here is 0.3 1/nm .

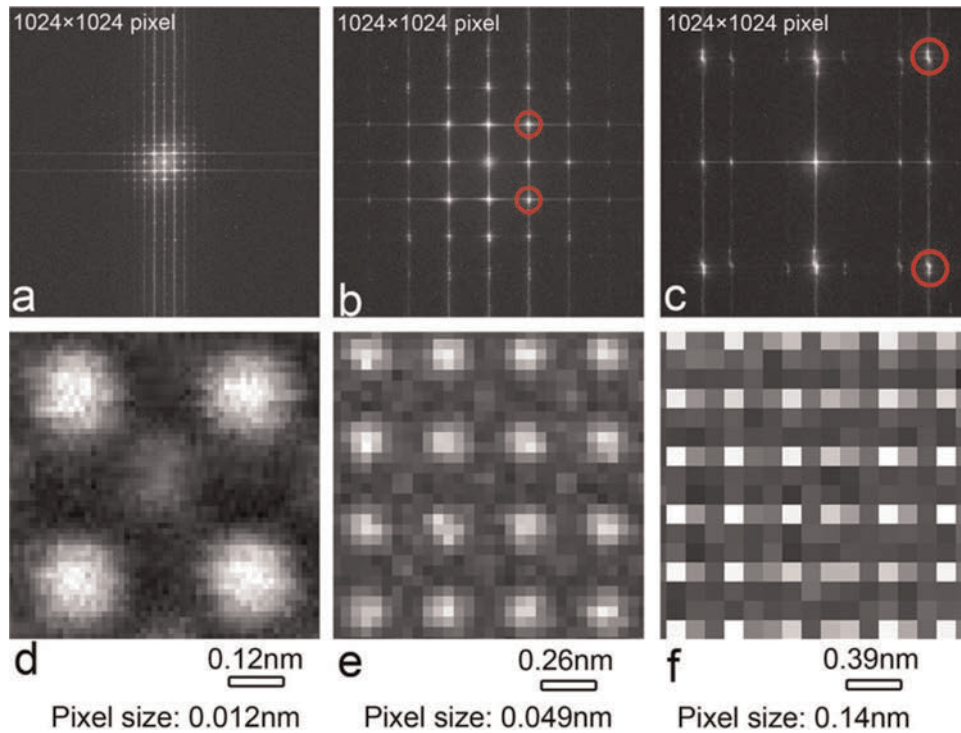


Fig. 5. Magnification presentations through FFT patterns and pixel size of AC-HAADF-STEM images used for strain analysis. (a)–(c) The full FFT patterns correspond to Fig. 2 (b), Fig. 3(a) and Fig. 4(a), respectively. Red circles in (b) and (c) denote the reciprocal lattice vector (101) and (10 $\bar{1}$) used for GPA analysis. (d) and (e) Magnified HAADF-STEM images show the pixel size directly, which also correspond to Fig. 2(b), Fig. 3(a) and Fig. 4(a). There is an aliasing effect in Fig. 5(c), which is common for low magnification lattice images recorded by a TEM, since low magnification lattice images are undersampled when digitized by an image recording system [45].

the whole layer structure under this low magnification. The size of this image is about 130 nm \times 115 nm, and the corresponding area of the raw image is more than 100 times than that of Fig. 2(b). For this magnification, it is impossible to identify the P_s configurations by inspecting δ_{Ti} in the PTO layers because it was completely concealed by the extremely big pixel size (will be further elaborated in Fig. 5(f)). However, horizontal strain (ϵ_{xx}) and vertical strain (ϵ_{yy}) as well as lattice rotations across the 180° domain-walls can still be extractable by GPA, as shown in Fig. 5(b)–(d). The uniform distribution of the ϵ_{xx} (Fig. 4(b)) and the obviously large c lattice parameter of PTO layers in the ϵ_{yy} (Fig. 4(c)) are consistent with Fig. 3(b) and (c), which reveal the validity of GPA for dealing with such low magnified image. For the lattice rotation mapping, line-profiles of two areas labeled with ‘1’ and ‘2’ were shown as insets in Fig. 4(d). The presence of three 180° domain-walls is observed, as seen both in the 2D mapping and the peaks in line-profile ‘1’ and ‘2’. Moreover, the 180° domain-wall in the lower PTO layer exhibits negative rotation, while the 180° domain-walls in the upper PTO layer exhibit both negative (left) and positive (right) rotations. Thus, the domain pattern of this multilayer shown in Fig. 4(a) can be determined, as the yellow arrows marked, which was confirmed by magnified AC-HAADF-STEM images (not shown here). However, under this extreme condition, only approximate information of the ferroelectric domain patterns could be affirmed, since the contrast of the 180° walls were rather blurred (Fig. 4(d)). Nevertheless, these preliminary messages could be useful for locating potential domain walls and further accurate analysis of strains and domain patterns.

In addition, more detailed information about the fine domain arrangements can be obtained by checking Fig. 4(a) with identified P_s configurations. Beside the PTO sandwiched thin SrTiO₃ layer, the P_s directions of local upper and lower PTO layers could adopt both ‘head-to-tail’ and ‘tail-to-tail’ arrangements, because of the non-collinear essence of the 180° domain-walls in the upper and lower PTO layers. To explore the physical insights of the PTO/STO

interactions and their influence on the property of this ferroelectric/paraelectric multilayer is an interesting topic for future investigations [44].

The full Fast Fourier Transform (FFT) patterns and the pixel sizes of Figs. 2(b), 3(a) and 4(a) are shown in Fig. 5. The continuously reduced magnifications of the three HAADF-STEM images can be realized by the progressive expansion of the FFT spots from Fig. 5 (a)–(c). In addition, the pixel size of the three images is visually shown in Fig. 5(d)–(f). As mentioned above, it is hard or impossible to identify the P_s directions in the PTO unit-cells by inspecting δ_{Ti} in Fig. 5(e) and (f) because it was completely concealed by the corresponding large pixel size. Even though, based on the reciprocal space information via GPA, it is easy to determine ferroelectric domain patterns for these low magnified images of PTO lattice (Figs. 3 and 4). In contrast, the δ_{Ti} is obvious only in Fig. 5 (d), which corresponds to highly magnified image (Fig. 2(b)) containing limited domain pattern information.

The combination of AC-HAADF-STEM and GPA is also applied to the strain measurements in a strained PbTiO₃/SrTiO₃ multilayer film, as shown in Fig. 6. The size of this image is about 102 nm \times 77 nm. The GdScO₃ substrate has a lattice parameter (\sim 0.397 nm) which is larger than the a lattice parameter of PTO [46]. The horizontal strain (ϵ_{xx}), vertical strain (ϵ_{yy}) and shear strain (ϵ_{xy}) as well as lattice rotation maps are shown in Fig. 6(b)–(e). Both the in-plane strain (ϵ_{xx}) and out-of-plane strain (ϵ_{yy}) exhibit inhomogeneous features. GPA lattice rotation map reveals interesting strain behaviors of such strained PbTiO₃/SrTiO₃ multilayer film, as shown in Fig. 6(d), where an obvious disclination character emerges. Moreover, both the 180° and 90° domain-walls are easily distinguishable in Fig. 6(d), thus the P_s directions of the domains are derived, as indicated by yellow arrows in Fig. 6(d). It is clearly seen that the tensile strain from the substrate cause unusual domain structures and resultant severe inhomogeneous strain distributions in the ferroelectric PTO layer, where the strain gradient can also be extracted [46]. Note that the 180° domain-

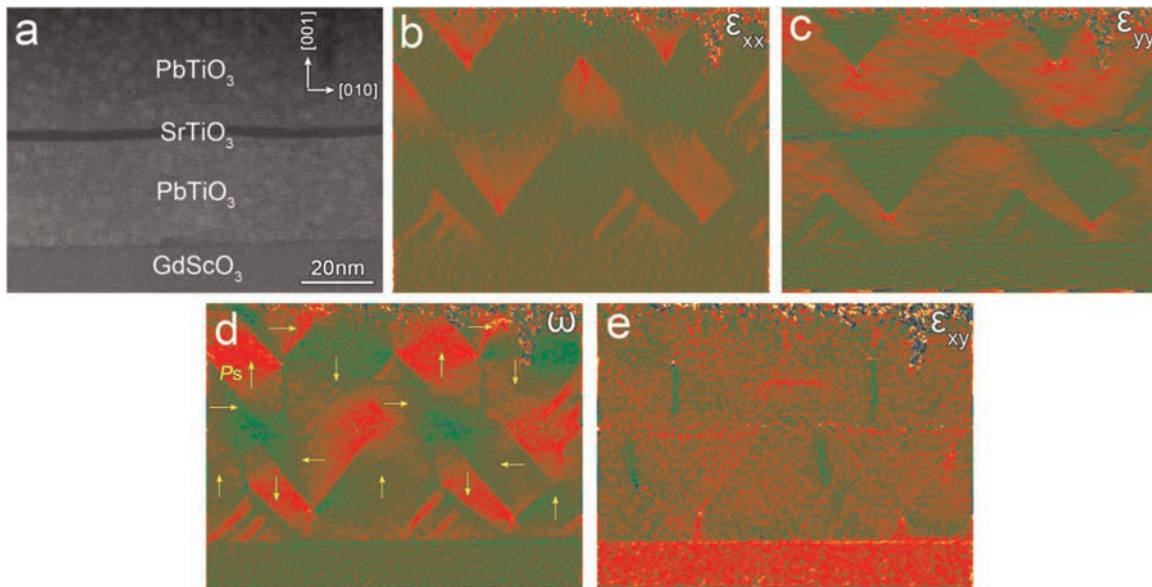


Fig. 6. Application of GPA for strain analysis of complex domain patterns in a strained $\text{PbTiO}_3/\text{SrTiO}_3/\text{PbTiO}_3$ multilayer film. (a) An AC-HAADF-STEM image. (b) In-plane strain ϵ_{xx} . (c) Out-of-plane strain ϵ_{yy} . (d) Lattice rotation mapping ω . (e) Shear strain ϵ_{xy} . The scanning direction is up to bottom. The radius of mask size used here is 0.6 1/nm.

walls can also be seen clearly in the shear strain map (Fig. 6(e), ϵ_{xy}). Nevertheless, the character of these domain patterns featured with special disclination strains cannot be immediately identified through the shear strain map. Thus we turn to use lattice rotation map and describe strain distributions in these ferroelectric films.

4. Discussion

Strain determination based on the combination of GPA and AC-HAADF-STEM imaging has shown great potential for analysis of ferroelectric domain patterns with high spatial resolution and over large areas. Although larger scale ferroelectric domain patterns can be efficiently determined by methods based on scanning probe microscopy (SPM) techniques, such as piezoresponse force microscopy (PFM) [12,47–49], the spatial resolution of these techniques is limited to several nanometers (5–30 nm) [12,47,48], which is far from nanometer accuracy like that in the present study. Particularly, dark field electron holography in a TEM is also well-adapted to measure strains over large fields of view with high spatial resolution [50]. Nevertheless, special hardware and operation mode are needed for performing this method. It is also worthwhile to mention that the acquisition duration of a HAADF-STEM image can be further doubled for getting a lower magnification image with extremely large image size, simultaneously the drifting effect is tremendously abated while the magnification is reduced. Based on this method, domain patterns of other ferroelectrics may also be determinable, such as domain structures in multiferroic BiFeO_3 [12,20,51].

We have shown in the above examples that HAADF-STEM imaging is a robust approach for strain analysis of ferroelectric materials exhibiting large strains, since the imaging conditions, such as specimen thickness and thickness gradient do not introduce contrast reversal effects [14,15,24,28]. Although the scanning error in HAADF-STEM mode is inevitable, this effect can be partially relieved by vertically rotating the scanning direction [23]. Particularly, the lattice rotation of 180° domain walls in PbTiO_3 can still be readily identified regardless of the presence of some scanning noises (Fig. 3(d)). Moreover, small crystal tilt generally induces homogeneous changing of intensity distributions of specific atom columns in AC-HAADF-STEM images, which should have little effect on the strain analysis based on GPA, because the

contrast of the image is systematically and evenly changed [18].

Based on the combination of GPA and AC-HAADF-STEM imaging, strain analysis can also be applied to investigate other strain-related phenomena. It is expected that large scale strains resulting from the interactions of defects in metals and large scale strain distributions in multilayer films/superlattice could be readily extracted. Such a benefit may facilitate the analysis of strain-related physical and chemical properties.

5. Conclusion

Large scale strain analysis is performed to $\text{PbTiO}_3/\text{SrTiO}_3$ multilayer by employing the combinations of GPA and AC-HAADF-STEM imaging. Both the development of lattice parameter and that of lattice rotation across the 180° domain-walls in PbTiO_3 are determined from the images with over $100 \text{ nm} \times 100 \text{ nm}$ dimensions. Moreover, by using the fingerprint effect of the lattice rotation as reference, domain patterns of the $\text{PbTiO}_3/\text{SrTiO}_3$ multilayers are successfully determined. The present study demonstrates the robustness of AC-HAADF-STEM imaging for large scale strain analysis, which is important for various strain-related property analyses like the ferroelectric domain configurations.

Acknowledgments

This work was supported by the National Natural Science Foundation of China (Grant nos. 51231007 and 51171190) and the National Basic Research Program of China (2014CB921002). Y.L. Tang gratefully acknowledges the IMR SYN-L.T.S. Kê Research Fellowship.

References

- [1] T. Fujita, P. Guan, K. McKenna, X. Lang, A. Hirata, L. Zhang, T. Tokunaga, S. Arai, Y. Yamamoto, N. Tanaka, Y. Ishikawa, N. Asao, Y. Yamamoto, J. Erlebacher, M. Chen, Atomic origins of the high catalytic activity of nanoporous gold, *Nat. Mater.* 11 (2012) 775–780.
- [2] F. Hÿe, M. Hÿtch, H. Bender, F. Houdellier, A. Clavier, Direct mapping of strain in a strained silicon transistor by high-resolution electron microscopy, *Phys. Rev. Lett.* 100 (2008) 156602.

- [3] C.-L. Jia, K.W. Urban, M. Alexe, D. Hesse, I. Vrejoiu, Direct observation of continuous electric dipole rotation in flux-closure domains in ferroelectric $\text{Pb}(\text{Zr,Ti})\text{O}_3$, *Science* 331 (2011) 1420–1423.
- [4] L. Houben, A. Thust, K. Urban, Atomic-precision determination of the reconstruction of a 90° tilt boundary in $\text{YBa}_2\text{Cu}_3\text{O}_{7-\delta}$ by aberration corrected HRTEM, *Ultramicroscopy* 106 (2006) 200–214.
- [5] M.D. Robertson, J.E. Currie, J.M. Corbett, J.B. Webb, Determination of elastic strains in epitaxial layers by HREM, *Ultramicroscopy* 58 (1995) 175–184.
- [6] R. Bierwolf, H. Hohenstein, F. Philipp, O. Brandt, G.E. Crook, K. Ploog, Direct measurement of local lattice distortions in strained layer structures by HREM, *Ultramicroscopy* 49 (1993) 273–285.
- [7] C.L. Johnson, M.J. Hÿtch, P.R. Buseck, Nanoscale waviness of low-angle grain boundaries, *Proc. Natl. Acad. Sci. U.S.A.* 101 (2004) 17936–17939.
- [8] M.J. Hÿtch, F. Houdellier, Mapping stress and strain in nanostructures by high-resolution transmission electron microscopy, *Microelectron. Eng.* 84 (2007) 460–463.
- [9] M.J. Hÿtch, J.-L. Putaux, J. Thibault, Stress and strain around grainboundary dislocations measured by high-resolution electron microscopy, *Philos. Mag.* 86 (2006) 4641–4656.
- [10] K.W. Urban, C.-L. Jia, L. Houben, M. Lentzen, S.-B. Mi, K. Tillmann, Negative spherical aberration ultrahigh-resolution imaging in corrected transmission electron microscopy, *Philos. Trans. R. Soc. A* 367 (2009) 3735–3753.
- [11] D.B. Williams, C.B. Carter, *Transmission Electron Microscopy A Textbook for Materials Science*, Springer, New York (2009), p. 483–506 (Chapter 28, Part 3: Imaging).
- [12] G. Catalan, J. Seidel, R. Ramesh, J.F. Scott, Domain wall nanoelectronics, *Rev. Mod. Phys.* 84 (2012) 119–156.
- [13] R.G. McQuaid, A. Gruverman, J.F. Scott, J.M. Gregg, Exploring vertex interactions in ferroelectric flux-closure domains, *Nano Lett.* 14 (2014) 4230–4237.
- [14] S.J. Pennycook, D.E. Jesson, High-resolution incoherent imaging of crystals, *Phys. Rev. Lett.* 64 (1990) 938–941.
- [15] S.J. Pennycook, D. Jesson, High-resolution Z-contrast imaging of crystals, *Ultramicroscopy* 37 (1991) 14–38.
- [16] A. De Backer, G.T. Martinez, A. Rosenauer, S. Van Aert, Atom counting in HAADF STEM using a statistical model-based approach: methodology, possibilities, and inherent limitations, *Ultramicroscopy* 134 (2013) 23–33.
- [17] M.F. Chisholm, S.J. Pennycook, Direct imaging of dislocation core structures by Z-contrast STEM, *Philos. Mag.* 86 (2006) 4699–4725.
- [18] S.E. Maccagnano-Zacher, K.A. Mkhoyan, E.J. Kirkland, J. Silcox, Effects of tilt on high-resolution ADF-STEM imaging, *Ultramicroscopy* 108 (2008) 718–726.
- [19] S.-Y. Chung, S.-Y. Choi, T. Yamamoto, Y. Ikuhara, Atomic-scale visualization of antisite defects in LiFePO_4 , *Phys. Rev. Lett.* 100 (2008) 125502.
- [20] C.T. Nelson, B. Winchester, Y. Zhang, S.-J. Kim, A. Melville, C. Adamo, C. M. Folkman, S.-H. Baek, C.-B. Eom, D.G. Schlom, L.-Q. Chen, X. Pan, Spontaneous vortex nanodomain arrays at ferroelectric heterointerfaces, *Nano Lett.* 11 (2011) 828–834.
- [21] S.V. Aert, K.J. Batenburg, M.D. Rossell, R. Erni, G.V. Tendeloo, Three-dimensional atomic imaging of crystalline nanoparticles, *Nature* 470 (2011) 374–377.
- [22] Y.-M. Kim, J. He, M.D. Biegalski, H. Ambaye, V. Lauter, H.M. Christen, S. T. Pantelides, S.J. Pennycook, S.V. Kalinin, A.Y. Borisevich, Probing oxygen vacancy concentration and homogeneity in solid-oxide fuel-cell cathode materials on the subunit-cell level, *Nat. Mater.* 11 (2012) 888–894.
- [23] G. Catalan, A. Lubk, A.H.G. Vlooswijk, G. Snoeck, C. Magen, A. Janssens, G. Rijnders, D.H.A. Blank, B. Noheda, Flexoelectric rotation of polarization in ferroelectric thin films, *Nat. Mater.* 10 (2011) 963–967.
- [24] D.A. Muller, Structure and bonding at the atomic scale by scanning transmission electron microscopy, *Nat. Mater.* 8 (2009) 263–270.
- [25] E.J. Kirkland, R.F. Loane, J. Silcox, Simulation of annular dark field stem images using a modified multislice method, *Ultramicroscopy* 23 (1987) 77–96.
- [26] P.M. Voyles, D.A. Muller, J.L. Grazul, P.H. Citrin, H.-J.L. Gossmann, Atomic-scale imaging of individual dopant atoms and clusters in highly n-type bulk Si, *Nature* 416 (2002) 826–829.
- [27] J.P. Buban, K. Matsunaga, J. Chen, N. Shibata, W.Y. Ching, T. Yamamoto, Y. Ikuhara, Grain boundary strengthening in alumina by rare earth impurities, *Science* 311 (2006) 212–215.
- [28] S.J. Pennycook, P.D. Nellist, *Scanning Transmission Electron Microscopy Imaging and Analysis*, Springer, New York (2011), p. 20–36 (Chapter 1).
- [29] J.M. LeBeau, S.D. Findlay, L.J. Allen, S. Stemmer, Quantitative atomic resolution scanning transmission electron microscopy, *Phys. Rev. Lett.* 100 (2008) 206101.
- [30] Yasutoshi Kotaka, Essential experimental parameters for quantitative structure analysis using spherical aberration-corrected HAADF-STEM, *Ultramicroscopy* 110 (2010) 555–562.
- [31] M.J. Hÿtch, E. Snoeck, R. Kilaas, Quantitative measurement of displacement and strain fields from HREM micrographs, *Ultramicroscopy* 74 (1998) 131–146.
- [32] M.J. Hÿtch, J.-L. Putaux, J.-M. Pénisson, Measurement of the displacement field of dislocations to 0.03 \AA by electron microscopy, *Nature* 423 (2003) 270–273.
- [33] M.J. Hÿtch, T. Plamann, Imaging conditions for reliable measurement of displacement and strain in high-resolution electron microscopy, *Ultramicroscopy* 87 (2001) 199–212.
- [34] J.L. Rouvière, E. Sarigiannidou, Theoretical discussions on the geometrical phase analysis, *Ultramicroscopy* 106 (2005) 1–17.
- [35] M. Arredondo, Q.M. Ramasse, M. Weyland, R. Mahjoub, I. Vrejoiu, D. Hesse, N. D. Browning, M. Alexe, P. Munroe, V. Nagarajan, Direct evidence for cation non-stoichiometry and Cottrell atmospheres around dislocation cores in functional oxide interfaces, *Adv. Mater.* 22 (2010) 2430–2434.
- [36] Y. Zhu, C. Ophus, J. Ciston, H. Wang, Interface lattice displacement measurement to 1 pm by geometric phase analysis on aberration-corrected HAADF STEM images, *Acta Mater.* 61 (2013) 5646–5663.
- [37] Y.L. Tang, Y.L. Zhu, Y.J. Wang, W.Y. Wang, Y.B. Xu, W.J. Ren, Z.D. Zhang, X.L. Ma, Atomic-scale mapping of dipole frustration at 90° charged domain walls in ferroelectric PbTiO_3 films, *Sci. Rep.* 4 (4115) (2014) 04115.
- [38] I. Tomeno, Y. Ishii, Y. Tsunoda, K. Oka, Lattice dynamics of tetragonal PbTiO_3 , *Phys. Rev. B* 73 (2006) 064116.
- [39] D. de Ligny, P. Richet, High-temperature heat capacity and thermal expansion of SrTiO_3 and SrZrO_3 perovskites, *Phys. Rev. B* 53 (1996) 3013–3022.
- [40] D.D. Fong, G.B. Stephenson, S.K. Streiffer, J.A. Eastman, O. Auciello, P.H. Fuoss, C. Thompson, Ferroelectricity in ultrathin perovskite films, *Science* 304 (2004) 1650–1653.
- [41] C.-L. Jia, S.-B. Mi, K. Urban, I. Vrejoiu, M. Alexem, D. Hesse, Atomic-scale study of electric dipoles near charged and uncharged domain walls in ferroelectric films, *Nat. Mater.* 7 (2008) 57–61.
- [42] P. Gao, C.T. Nelson, J.R. Jokisaari, S.-H. Baek, C.W. Bark, Y. Zhang, E. Wang, D. G. Schlom, C.-B. Eom, X. Pan, Revealing the role of defects in ferroelectric switching with atomic resolution, *Nat. Commun.* 2 (591) (2011) 1600.
- [43] B. Meyer, D. Vanderbilt, Ab initio study of ferroelectric domain walls in PbTiO_3 , *Phys. Rev. B* 65 (2002) 104111.
- [44] P.A. Puente, P.G. Fernández, J. Junquera, Interplay of couplings between antiferrodistortive, ferroelectric, and strain degrees of freedom in monodomain $\text{PbTiO}_3/\text{SrTiO}_3$ superlattices, *Phys. Rev. Lett.* 107 (2011) 217601.
- [45] P.J.B. Koeck, Ins and outs of digital electron microscopy, *Microsc. Res. Tech.* 49 (2000) 217–223.
- [46] Y.L. Tang, Y.L. Zhu, X.L. Ma, A.Y. Borisevich, A.N. Morozovska, E.A. Eliseev, W. Y. Wang, Y.J. Wang, Y.B. Xu, Z.D. Zhang, S.J. Pennycook, Observation of a periodic array of flux-closure quadrants in strained ferroelectric PbTiO_3 films, *Science* 348 (2015) 547–551.
- [47] M. Abplanalp, L.M. Eng, P. Günter, Mapping the domain distribution at ferroelectric surfaces by scanning force microscopy, *Appl. Phys. A* 66 (1998) S231–S234.
- [48] S.V. Kalinin, B.J. Rodriguez, S. Jesse, E. Karapetian, B. Mirman, E.A. Eliseev, A. N. Morozovska, Nanoscale electromechanics of ferroelectric and biological systems: a new dimension in scanning probe microscopy, *Annu. Rev. Mater. Res.* 37 (2007) 189–238.
- [49] K.L. Kim, N.T. Tsou, J.E. Hubera, Domain evolution processes during poling of a near-morphotropic $\text{Pb}(\text{Zr,Ti})\text{O}_3$ ceramic, *J. Appl. Phys.* 113 (2013) 194104.
- [50] M. Hÿtch, F. Houdellier, F. Hÿe, E. Snoeck, Nanoscale holographic interferometry for strain measurements in electronic devices, *Nature* 453 (2008) 1086–1089.
- [51] W.Y. Wang, Y.L. Tang, Y.L. Zhu, Y.B. Xu, Y. Liu, Y.J. Wang, S. Jagadeesh, X.L. Ma, Atomic Level 1D structural modulations at the negatively charged domain walls in BiFeO_3 films, *Adv. Mater. Interfaces* 2 (2015) 1500024.